American Mineralogist, Volume 96, pages 1480–1489, 2011

Estimating compositions of natural ringwoodite in the heavily shocked Grove Mountains 052049 meteorite from Raman spectra

L. Feng,[1,2] Y. Lin,[1,*] S. Hu,[1,2] L. Xu,[3] and B. Miao[4]

[1]Key Laboratory of the Earth's Deep Interior, Institute of Geology and Geophysics, Chinese Academy of Sciences, Beijing 100029, China
[2]Graduate School of Chinese Academy of Sciences, Beijing 100118, China
[3]National Astronomical Observatory, Chinese Academy of Sciences, Beijing 100029, China
[4]Department of Resources and Environmental Engineering, Guilin University of Technology, Guilin 541004, China

Abstract

A combined Raman spectroscopy and electron probe microanalysis study of the heavily shocked Grove Mountains (GRV) 052049 meteorite revealed the largest chemical fractionation of natural ringwoodite, and composition-dependent variation of the intensities and/or wavenumbers of Raman bands. With Fa content [atomic ratio of Fe/(Fe+Mg)] of ringwoodite varying from 27.8 to 81.6 mol%, the peak position of the single band around 290 cm^{-1} (SB1), which relates to the SiO_4 translation mode, shifts from 296.0 to 284.6 cm^{-1}, and one of the doublets around 790 cm^{-1} (DB1), which relates to the symmetric stretching of SiO_4, shifts from 796.3 to 782.7 cm^{-1}. In addition, the relative intensities of SB1 and the other band of the doublet around 840 cm^{-1} (DB2), which relates to asymmetric stretching of SiO_4, increases with Fa content. Based on the paired Raman-EPMA data, single-peak and two-peak calibrations were established, which can be used to derive Fa contents of ringwoodite from the Raman spectra. The accuracy of Raman-derived Fa content of ringwoodite is better than ±5 mol%. The correlation of SB1 intensity with the Fa content of ringwoodite suggests that the vibration of SB1 is enhanced with the substitution of Mg^{2+} by Fe^{2+}. The correlation between Raman spectra and the chemical composition of ringwoodite have potential applications in on-line measurement of high-pressure experiments and in situ mineralogical determination in future planetary explorations.

Keywords: Raman spectroscopy, ringwoodite, chemical compositions, shocked meteorite

Introduction

As pressure increases, olivine, α-$(Mg,Fe)_2SiO_4$, is transformed to wadsleyite (β phase) at 13–16 GPa (at 1200 °C) and then ringwoodite, γ-$(Mg,Fe)_2SiO_4$, at 18–22 GPa (at 1200 °C) (Katsura and Ito 1989; Agee 1998). Both of the high-pressure polymorphs are predicted to be the predominant minerals in the Earth's transition zone (400–660 km), and ringwoodite is predicted to occur in the lower part (Ringwood 1991). Thermodynamical, physical, and crystallographic properties of ringwoodite have been extensively studied to understand the dynamical processes of the Earth's mantle and to determine properties of the lower part of transition zone. Raman spectra are related to the lattice vibration and are critical for identifying ringwoodite (Guyot et al. 1986; Yamanaka and Ishii 1986; McMillan and Akaogi 1987; Chopelas et al. 1994). However, little attention has been devoted to the effect of substitution of cations on the lattice vibration. McMillan and Akaogi (1987) noticed a significant shift of the lowest-frequency F_{2g} mode of Ni_2SiO_4 spinel (190 cm^{-1}) in comparison to γ-Mg_2SiO_4 (302 cm^{-1}) and interpreted this shift as a result of substitution of Ni^{2+} by Mg^{2+}. Later study showed that the different translations of SiO_4 and M^{2+} are strongly coupled (Chopelas et al. 1994).

Previous studies of Raman spectra of olivine revealed a correlation between the Raman band shift and chemical composition, which was used to extract chemical compositions of the olivine-group minerals (fayalite content) (Kuebler et al. 2006; Mouri and Enami 2008). Analog studies were extended to pyroxenes (Wang et al. 2001), chromite (Al, Fe, Cr cation substitution), ilmenite (Fe, Ti), hematite (Fe, Ti) (Wang et al. 2004), and feldspars (Na, K, Ca) (Freeman et al. 2003, 2008). These studies provided unique and promising methods for space exploration to estimate both mineralogical and compositional information with the Raman spectrometer. In principle, the chemical composition of ringwoodite can also be determined from its Raman spectra if a calibration between them can be established. However, the effects of cation substitution between Mg^{2+} and Fe^{2+} on the vibrational mode frequencies of ringwoodite are unknown.

Natural ringwoodite has been found only in severely shocked meteorites, formed by solid-solid transformation of olivine (e.g., Putnis and Price 1979; Chen et al. 1996; Ohtani et al. 2004; Xie and Sharp 2007) or crystallization from olivine melts (Miyahara et al. 2008a, 2009) under high-pressure conditions created by impact events on planets or asteroids. Many ringwoodite grains in L-group chondrites have homogeneous compositions with a narrow range of fayalite contents ($Fa_{26–28}$), overlapping with the composition of olivine in the same host meteorites (Putnis

* E-mail: linyt@mail.igcas.ac.cn

and Price 1979; Ohtani et al. 2004). Recently, ringwoodite with variable compositions ($Fa_{28–38}$) was reported as evidence for crystallization from shock-induced olivine melts (Miyahara et al. 2008, 2009). The compositional variation of ringwoodite from the Moon and within asteroids is primarily caused by Mg^{2+} and Fe^{2+} substitution. We found the largest compositional range of ringwoodite ($Fa_{28–81}$) within the same meteorite to date, thus providing a unique opportunity to study the lattice vibration related to Mg^{2+}-Fe^{2+} substitution. Based on study of a shocked meteorite, we report the correlation between Raman shifts and Fe/(Mg + Fe) cation ratios of natural ringwoodite. This correlation can provide information on the lattice vibration modes, as well as the possibility to determine both the mineral phase and chemical composition solely by Raman spectroscopy. As an example, we present a method of calibration between Raman spectra and chemical composition of ringwoodite and discuss its potential application to high-pressure experiments and space exploration. The textural and compositional features of ringwoodite grains and variations in their Raman spectra were reported in preliminary works (Feng et al. 2007; Feng and Lin 2008).

Experiments

A polished thin section of GRV 052049 was studied with a LEO 1450VP scanning electron microscope (SEM) equipped with a backscattered electron (BSE) detector adjusted for high contrast and an energy-dispersive spectrometer (EDS) at the Institute of Geology and Geophysics, Chinese Academy of Sciences. The microtextures of ringwoodite grains were also investigated using a JEOL JSM-71010 field emission scanning electron microscope (FE-SEM) operating at an acceleration voltage of 15 kV. An ultra-thin (120–130 nm) slice from ringwoodite grains was extracted by a focused ion beam (FIB) system JEOL JEM-9320. The preparation of FIB slice was according to Miyahara et al. (2008b). The textures and chemical compositions of coexisting ringwoodite crystallites were investigated by a scanning transmission electron microscopy (STEM), JEOL JEM-3000F operating at 300 kV and equipped with a JOEL energy-dispersive X-ray spectrometer (EDS). The compositions obtained by EDS under STEM mode were corrected using experimentally determined κ-factors (San Carlos olivine). The FE-SEM and FIB-STEM work was conducted in Tohoku University.

Assemblages with large (a few micrometers) and relatively homogeneous crystals of ringwoodite were selected for Raman and electron probe microanalyzer (EPMA) measurement at the Institute of Geology and Geophysics, Chinese Academy of Sciences. Backscattered electron (BSE) images for each assemblage documented the analysis positions of the combined Raman and compositional analyses. Quantitative analyses of the selected grains of ringwoodite were done using a JXA 8100 type EPMA with four wavelength-dispersive spectrometers, a 20 nA accelerating voltage, 15 kV beam current, and a 1 μm beam diameter. Diopside (Ca and Si), jadite (Na), almandine garnet (Fe and Al), orthoclase (K), rhodonite (Mn), forsterite (Mg), synthetic escolaite (Cr), and rutile (Ti) were used as standards. The standard ZAF matrix correction program was applied to calculate the chemical compositions.

Examination of BSE images enabled the Raman spectra of the selected ringwoodite grains to be measured at the same EPMA positions. The Laser Raman spectrometer used in this study was a Renishaw RM-2000 type, with a confocal microscope and a 50× long-working distance objective lens. An Ar ion laser with 514.5 nm wavelength was used as the excitation source, which produces an unpolarized, focused beam of ~1 μm diameter on the surface of sample. The power of the laser is 20 mW. Before measurement, the Laser Raman spectrometer was calibrated with a single-crystal silicon standard to the standard band at wavenumber 520.5 cm^{-1}. The resolution of the Raman spectrum is 1.67 cm^{-1}. Replicated measurements were conducted three times on the same position. The Raman bands did not show any shifts in vibrational frequencies, which indicate that the well-crystallized ringwoodite grains did not suffer any laser heating effects at this level of laser power. Each analysis of the Raman spectrum was accumulated for the three runs with a total integration time of 60–90 s.

Following measurement, the Raman peak positions were determined by Origin 7.5 software, using a least-squares curve fitting method. The Lorentzian peak model and a linear baseline were used to fit the Raman peaks. We used a constraint-free iteration option for all parameters (e.g., peak position, height, width, and slope, and intercept of a linear baseline), and the fitting calculation ended at convergence (or a minimum). Reproducibility of the peak positions is better than 0.2 cm^{-1}.

Sample and occurrence of ringwoodite

All grains of ringwoodite were found in the GRV 052049 meteorite recovered in Grove Mountains, Antarctica, by the 22nd Chinese Antarctic Research Expedition. This meteorite weighs 96.7 g and was originally classified as an L5 chondrite. It experienced severe shock metamorphism and was partially melted to produce melt veins. Ringwoodite occurs in rounded or ovoid silicate fragments entrained in the veins and/or is in the host rock in contact with the veins. A vein-bearing slice of this meteorite was made into a polished thin section for this study.

Figure 1 shows dark shock-induced melt veins (up to >3 mm wide) in the polished thin section under transmitted light. Numerous irregular transparent fragments entrained in the dark vein matrix contain ringwoodite and various high-pressure polymorphs of pyroxenes and plagioclase. Most ringwoodite grains occur as rims (2–10 μm thin) of rounded or ovoid ringwoodite-olivine assemblages (Fig. 2). Ringwoodite appears as light gray [hence high Fe/(Fe+Mg) ratios] in the BSE images, in sharp contrast with the dark and heterogeneous cores [low Fe/(Fe+Mg) ratios], which generally exhibit a dendrite-like texture (Figs. 2a and 2c). Bright irregular crystals (<1 μm) embedded in the FeO-depleted polycrystalline dendrites were also noticed (Figs. 2b and 2c). However, only Raman bands of olivine were determined in the dark core regions. EMPA analyses of the olivine cores give a compositional range of $Fa_{7–12}$. In addition to the rim occurrence, ringwoodite was found as rounded islands in the interiors of large ringwoodite-olivine assemblages (up to 700 μm).

Most of the ringwoodite rims and islands are polycrystalline, consisting of micrometer-sized grains of ringwoodite (up to 5 μm in size). Although the BSE image brightness of different ringwoodite islands varies from grain to grain, individual grains, as well as ringwoodite rims of each assemblage, are relatively homogeneous (Figs. 2b and 2d). However, slight variations in brightness among the ringwoodite crystallites were noticed under high-contrast BSE mode. To clarify the compositional uniformity of ringwoodite islands and rims, several regions were selected for replicated EMPA measurements (3–4 times). Variations in Fa-values from the same areas range from 0.1–2.1 mol%. STEM-

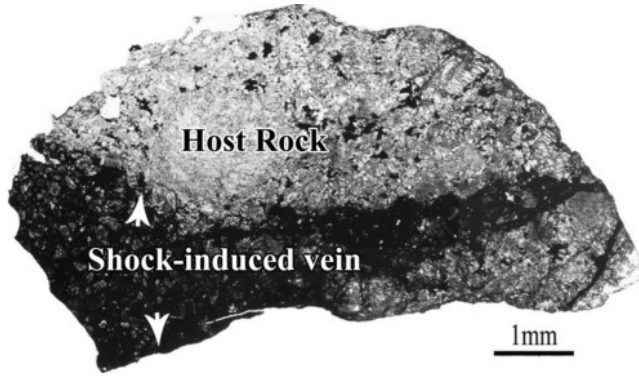

Figure 1. An overview photo of GRV 052049 under polarized light, showing the dark shock-induced melt veins. The scale bar is 1 mm.

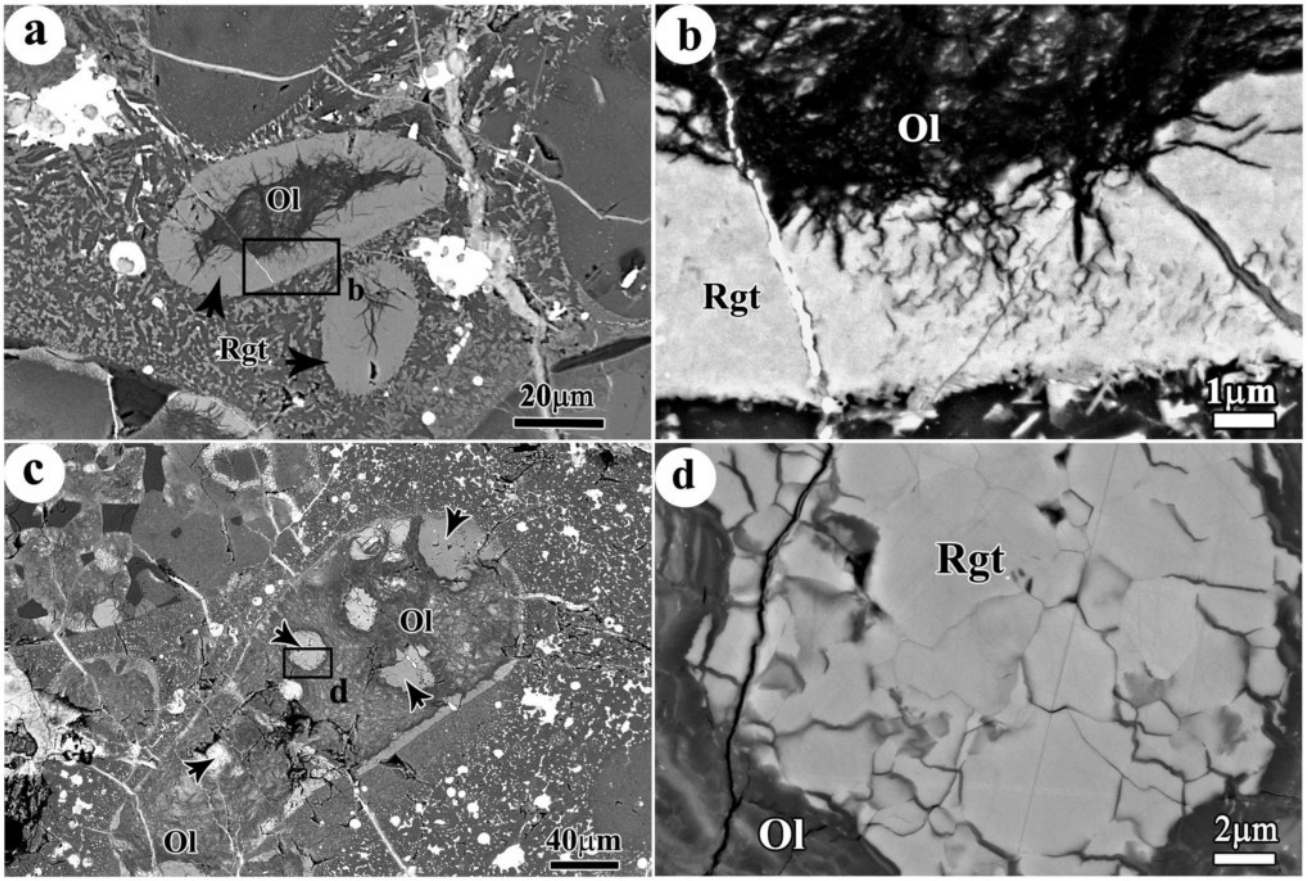

FIGURE 2. BSE images of various occurrences of ringwoodite. (**a**) Ringwoodite (Rgt) occurs as a bright rim on the darker, dendritic olivine core. The width of the view is 220 μm. (**b**) FE-SEM image of the black box in **a**. The dark, upper part in the view is mainly composed of polycrystalline olivine (Ol), within which bright irregular crystallites with sizes less than 1 μm were also discovered. The ringwoodite rim (lower part in the view) is generally homogeneous, with some parts penetrated by dark, polycrystalline olivine offshoots. The width of the view is 16 μm. (**c**) An olivine-ringwoodite assemblage contains ringwoodite islands inside an olivine-rich core. Black arrows point to ringwoodite. The different brightness of ringwoodite grains reflects their various compositions. The coexisting Fe-depleted olivine areas (Ol) depict heterogeneous brightness, as submicrometer-sized bright crystallites embedded in dark grains. The width of the view is 600 μm. (**d**) A close-up FE-SEM image of the inset in **c**. The ringwoodite island is composed of micro-sized crystals of identical compositions. The width of the view is 33 μm.

EDS analyses of a FIB-TEM slice containing a ringwoodite island revealed that the variation of Fa contents of neighboring ringwoodite crystallites is no more than 3 mol%. Based on the above measurements, we consider that the ringwoodite islands and rims, which were chosen for this study, are mostly composed of ringwoodite crystallites whose compositions are homogeneous in a scale of 3 mol%.

Furthermore, the ringwoodite rims and islands are commonly penetrated by dark and fiber-like olivine. Hence, homogeneous areas of ringwoodite, located away from the olivine offshoots, were carefully selected for the combined EPMA-Raman analysis to eliminate effects of possible shift of the beams and to avoid contamination from the coexisting olivine.

CHEMICAL COMPOSITIONS AND RAMAN SPECTRA OF RINGWOODITE

GRV 052049 is an L5 chondrite. The host rock silicates are relatively homogeneous, with the Fa content of olivine ranging from 23.5 to 25.0 mol% (avg. 24.0 ± 0.4 mol%) and the Fs content [atomic ratio of Fe/(Fe+Mg)] of low-Ca pyroxene ranging from 20.3 to 22.0 mol% (avg. 20.6 ± 0.5 mol%). In addition, ringwoodite shows a large compositional range with Fa contents ranging from 27.8 to 81.6 mol%.

Eighty analyses of ringwoodite were collected from the same positions where Raman spectra were integrated. Atomic ratios of the cations were calculated based on a stoichiometric formula of $A_2[BO_4]$ for ringwoodite. Tetrahedral B-site cations are Si^{4+}, Ti^{4+}, and Al^{3+}, whereas octahedral A-site cations are Mg^{2+}, Fe^{2+}, Ca^{2+}, Mn^{2+}, and Cr^{3+}. In addition to Mg^{2+} and Fe^{2+}, other cations in the octahedral sites are negligible (<0.5%), such that the Fa content of ringwoodite is determined as Fa mol% = Fe/(Fe+Mg) × 100%. Representative analyses of ringwoodite are given in Table 1.

The silicate spinel γ-$(Mg,Fe)_2SiO_4$ belongs to the space group $O7/h$ ($Fd3m$, $Z = 8$). Forty-two vibrational modes are expected from the primitive cell and can be divided among the following symmetry species

$$A_{1g}(R) + E_g(R) + 3F_{2g}(R) + 2A_{2u} + 2E_u + 4F_{1u}(IR) + 2F_{2u}. \quad (1)$$

TABLE 1. Representative EMPA analyses on ringwoodite grains in GRV 052049

No.	11-25		12-14		13-1	4-8		11-4		12-12		7-2	3-10	11-14	
	avg. n=4	SD	avg. n=4	SD	n=1	avg. n=5	SD	n=2	SD	n=4	SD	n=1	n=1	avg. n=2	SD
SiO_2	32.26	0.64	33.04	0.68	36.86	37.78	0.70	35.68	0.23	33.64	0.57	37.44	33.71	31.35	1.04
TiO_2	0.02	0.02	0.00	0.01	0.00	0.01	0.01	0.00	0.00	0.02	0.02	0.00	0.02	0.00	0.00
Al_2O_3	0.01	0.01	0.02	0.02	0.00	0.01	0.01	0.07	0.01	0.01	0.01	0.00	0.02	0.09	0.10
Cr_2O_3	0.10	0.01	0.22	0.12	0.09	0.16	0.06	0.00	0.00	0.18	0.03	0.12	0.06	0.47	0.52
FeO*	55.87	0.71	50.55	0.81	34.21	26.66	0.61	38.09	0.37	48.58	0.86	28.44	47.72	59.29	2.25
MnO	0.06	0.01	0.06	0.03	0.00	0.02	0.02	0.03	0.03	0.04	0.03	0.00	0.05	0.11	0.03
MgO	11.94	0.36	16.68	0.56	29.04	36.59	0.45	26.40	1.27	18.03	0.07	33.16	18.88	8.27	0.14
CaO	0.01	0.02	0.01	0.01	0.00	0.01	0.01	0.01	0.00	0.15	0.15	0.00	0.01	0.00	0.00
Na_2O	0.00	0.00	0.02	0.01	0.06	0.01	0.01	0.00	0.00	0.01	0.01	0.03	0.02	0.01	0.02
K_2O	0.01	0.00	0.00	0.00	0.03	0.00	0.00	0.01	0.01	0.01	0.01	0.00	0.00	0.00	0.00
Totals	100.28		100.60		100.28	101.25		100.30		100.66		99.19	100.50	99.60	
Si	0.997	0.017	0.989	0.022	1.011	0.989	0.016	0.999	0.020	0.994	0.014	1.010	0.993	0.999	0.024
Ti	0.000	0.000	0.000	0.000	0.000	0.000	0.000	0.000	0.000	0.000	0.000	0.000	0.000	0.000	0.000
Al	0.000	0.000	0.001	0.001	0.000	0.000	0.000	0.002	0.000	0.000	0.000	0.000	0.001	0.004	0.004
Cr	0.002	0.000	0.005	0.003	0.002	0.003	0.001	0.000	0.000	0.004	0.001	0.003	0.001	0.012	0.013
Fe^{2+}	1.445	0.022	1.265	0.017	0.785	0.584	0.014	0.892	0.003	1.201	0.022	0.642	1.176	1.581	0.075
Mn^{2+}	0.002	0.000	0.001	0.001	0.000	0.001	0.000	0.001	0.001	0.001	0.001	0.000	0.001	0.003	0.001
Mg	0.550	0.016	0.744	0.023	1.188	1.432	0.019	1.102	0.038	0.795	0.005	1.333	0.829	0.393	0.003
Ca	0.000	0.001	0.000	0.000	0.000	0.000	0.000	0.000	0.000	0.005	0.005	0.000	0.000	0.000	0.000
Na	0.000	0.000	0.001	0.001	0.003	0.000	0.000	0.000	0.000	0.000	0.001	0.002	0.001	0.001	0.001
K	0.000	0.000	0.000	0.000	0.001	0.000	0.000	0.000	0.000	0.000	0.000	0.000	0.000	0.000	0.000
Total	2.998		3.006		2.990	3.010		2.997		3.001		2.989	3.005	2.993	
Fa†	72.4	0.007	63.0	0.008	39.8	28.9	0.006	44.7	0.009	60.2	0.005	32.5	58.6	80.1	0.008

Note: SD is standard deviation calculated from multiple measurements.
* All Fe assumed to be Fe^{2+}.
† Fa = Fe/(Fe+Mg) molar × 100.

There are five Raman active modes ($A_{1g} + E_g + 3F_{2g}$), each attributed to internal vibration modes of the tetrahedral SiO_4 units, and each have been observed on synthetic γ-$(Mg,Fe)_2SiO_4$ at ambient conditions (Akaogi et al. 1984; McMillan and Akaogi 1987; Chopelas et al. 1994).

Figure 3 shows representative Raman spectra of ringwoodite grains from GRV 052049 in comparison with a typical synthesized γ-Mg_2SiO_4 from Chopelas et al. (1994). The dominant feature of the spectrum, illustrated for both the natural ringwoodite and synthesized γ-Mg_2SiO_4, is the strong doublet peaks ~790 cm^{-1} (referred as DB1) and ~840 cm^{-1} (referred as DB2). A less strong single band ~300 cm^{-1} (referred as SB1) is also observed in both the synthetic and natural ringwoodite. Other bands at ~370 and ~600 cm^{-1} are weak and not observed in all the natural ringwoodite samples. Hence, only the bands DB1, DB2, and SB1 were measured for peak positions and peak heights, which are commonly used to represent the peak intensities.

The peak positions of SB1 and DB1 and the intensities of SB1 and DB2 of ringwoodite from GRV 052049 show significant variation when correlated to composition (Fig. 4). As the Fa content increases from 27.8 to 81.6 mol%, SB1 shifts from 296.0 to 284.6 cm^{-1}, and DB1 from 796.3 to 782.7 cm^{-1}. The peak position of DB2 shows some variation (841.0–849.3 cm^{-1}), but without significant correlation to Fa content.

The intensity of DB1 remains nearly the constant as the Fa content varies from 28 to 81 mol% (Fig. 4). Setting DB1 as a reference, the relative intensity of DB2 increases from 0.33 to 1.45 with an increase in Fa content. The same trend in the relative intensity of SB1 to DB1 was also encountered, varying from 0.15 to 1.00 as the Fa content increased from 28 to 81 mol%. The systematic variation of Raman spectra of ringwoodite with respect to its composition suggests that it is possible to estimate the latter from the former, if a calibration can be established.

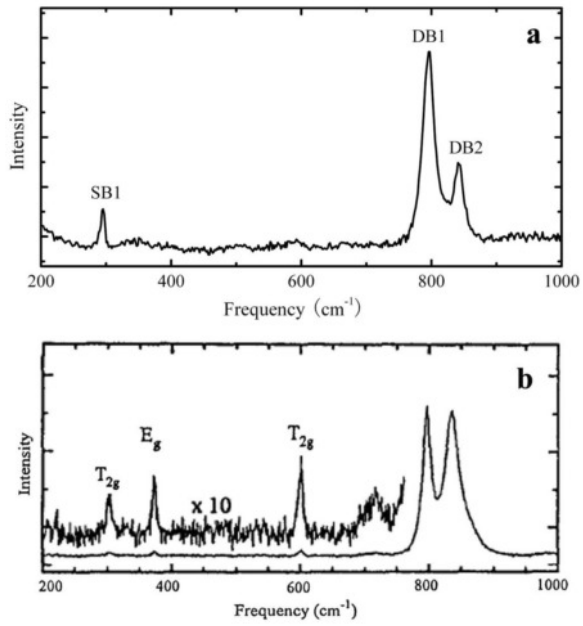

FIGURE 3. Raman spectra of ringwoodite. (**a**) GRV 052049, (**b**) synthetic γ-Mg_2SiO_4 (Chopelas et al. 1994). The characteristic Raman peaks of ringwoodite are present in both of the spectra, and referred as SB1, DB1, and DB2, respectively.

CALIBRATION OF FA CONTENT OF RINGWOODITE

Eighty pairs of EMPA and Raman analyses were obtained from the entire thin section, and are inferred to be a "full data set." Since the construction of a calibration between Raman spectra and chemical compositions of ringwoodite requires higher quality data, we re-examined all of the data and selected only pairs that exhibit good stoichiometry (analytical total between 99 and 102 wt%, cation sum between 2.98–3.00 for 6 O atoms) and good

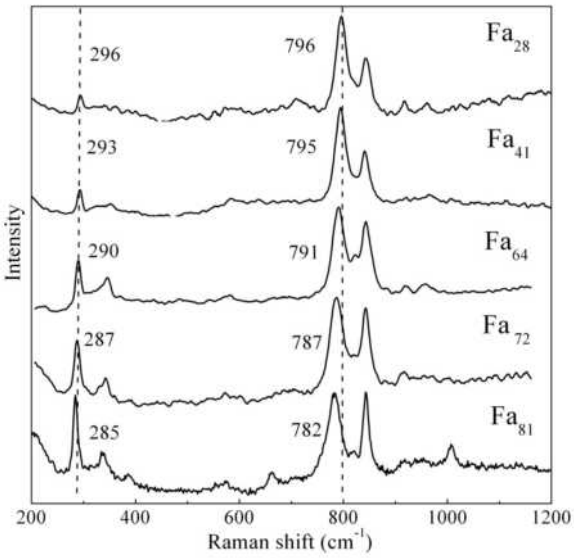

FIGURE 4. Representative Raman spectra of ringwoodite with various chemical compositions. Both SB1 and DB1 shift systematically toward lower wavenumbers with an increase in Fa content.

resolution of both SB1 and DB1. Raman spectra having strong olivine bands were excluded.

Based on above criterion, 28 pairs of analyses (Table 2) were chosen as a "selected data set," to create the calibration. Furthermore, both the full data set and selected data set were used to evaluate the calibration by plotting the Raman-derived Fa contents (calculated from calibration equations) against the Fa values determined by EMPA to measure the overall accuracy of this method.

The selected data set is plotted in Figure 5. The peak positions of SB1 and DB1 are well correlated to the chemical compositions (Figs. 5a and 5b). The relative peak heights of SB1 to DB1 and DB2 to DB1 also increase systematically as a function of Fa values (Figs. 5c and 5d). However, the full data set illustrates that the relative peak heights show large deviations over some ranges of composition. Raman peak intensities are more affected by other factors, e.g., crystal orientations or overlapping by Raman peaks (~820 and ~840 cm^{-1}) from neighboring olivine grains. In addition, determinations of peak heights are also dependent on the baseline-subtracting and curve-fitting procedure on the spectra. Therefore, we propose to only use the peak positions of SB1 and DB1 to predict the chemical composition of ringwoodite.

Single-peak calibration

The correlation between Fa contents and peak positions of SB1 and DB1 (Figs. 5a and 5b, respectively) can be expressed as:

$$\text{Fa (mol\%)} = y_i + a_i x_i + b_i x_i^2 \quad (2)$$

where i refers to peak of SB1 or DB1, x_i to the peak position, y_i to the intercept, and a_i and b_i to the coefficients listed in Table 3.

To estimate the uncertainty of the Fa content of ringwoodite acquired from the Raman spectra, we plotted the Fa values determined by EMPA against those calculated from SB1 and DB1 peak positions using Equations 1 and 2 (Figs. 6a and 6b). The error bars of the Raman-derived Fa values were calculated from the standard deviation of replicate curve-fitting analyses of individual spectrum (6–10 times), and the reproducibility of peak positions are usually better than 0.2 cm^{-1}. The error bars of the Fa values by EMPA are the standard deviation of multi-measurements on the same grains. It should be noticed that the DB1 calibration (Fig. 6b, slope = 1.00, $R^2 = 0.995$) is better than SB1 calibration (Fig. 6a, slope = 0.98, $R^2 = 0.989$) as the points in the latter are slightly more scattered across the whole range. The 95% confidence intervals for DB1 are tighter than for the SB1 calibration. Six of the 28 selected analyses fall outside the confidences intervals in DB1, whereas 10 do for SB1.

There are several reasons for discrepancies of Raman-derived Fa values from EMPA results: different crystal orientations of the ringwoodite grains, which may cause variations in Raman peak positions as well as peak intensities; relatively low signal-to-noise ratios of the rock specimen and various degree of crystallinity of ringwoodite crystallites, which would affect uncertainty in defining peak positions; and differences in the sampling volume between Raman and EMPA. The penetration of the Raman laser (several micrometers) is deeper than the electron beam (~1.4 μm under the conditions for this study) (Potts 1987; Haskin et al. 1997), so the Raman spectra may sample a deeper part of the grain. Natural samples are, to some extent, relatively heterogeneous; therefore the difference in the sampling volume between the two techniques may influence the accuracy of the Raman-derived Fa values. Furthermore, the DB1 peak is higher than SB1, e.g., for the Fa_{20-40} grains, the intensity of SB1 is less than 1/3 of DB1 such that the peak positions of DB1 should be more accurately determined by spectral curve-fit procedures. Therefore, the DB1 calibration is more accurate than the SB1 calibration, and the latter shows more deviation in the Fe-poor regions.

TABLE 2. EMPA and Raman results of the selected data set

No.	Fa values (mol%)	Peak positions (cm^{-1})			Relative peak heights	
		SB1	DB1	DB2	SB1 to DB1	DB2 to DB1
1-R5	81.6	284.6	782.7	843.2	0.97	1.45
11-15	80.9	285.0	783.6	844.0	0.91	0.94
11-14	80.1	285.5	784.0	842.9	1.00	1.41
12-16	78.5	286.4	784.9	844.5	0.90	1.35
11-26	72.6	287.4	786.0	844.4	0.74	0.97
12-1	72.0	287.7	786.7	843.0	0.67	0.83
11-24	68.1	288.3	788.0	844.1	0.62	0.95
11-3	66.9	288.9	788.3	843.7	0.66	0.97
11-1	66.7	288.6	788.2	844.9	0.75	0.9
10-5	65.2	288.8	788.5	843.9	0.71	0.88
12-14	63.0	289.0	789.3	843.0	0.58	0.76
12-12	60.2	290.1	791.1	843.2	0.51	0.83
12-17	58.6	290.9	791.2	846.2	0.52	0.82
21-R3	55.6	290.3	791.8	841.9	0.47	0.63
1-R4	54.0	290.6	792.7	841.8	0.44	0.63
13-R2	47.7	292.2	794.3	841.9	0.35	0.61
11-12	46.3	293.2	793.9	843.4	0.32	0.61
11-4	44.7	292.7	794.3	844.6	0.35	0.76
5-3	43.6	292.9	794.1	842.0	0.31	0.47
8-1	41.1	292.8	794.7	841.2	0.31	0.51
13-1	39.8	294.2	795.4	842.9	0.27	0.83
1-5	38.9	293.4	795.2	841.0	0.26	0.47
1-1	36.7	294.2	795.6	842.3	0.24	0.44
1-6	35.3	294.7	796.3	842.3	0.20	0.46
5-5	33.3	294.6	796.1	841.4	0.22	0.43
6-9	32.4	295.2	796.0	841.5	0.22	0.4
6-11	31.8	295.0	796.7	842.4	0.19	0.36
4-8	28.9	297.6	797.5	843.5	0.15	0.33

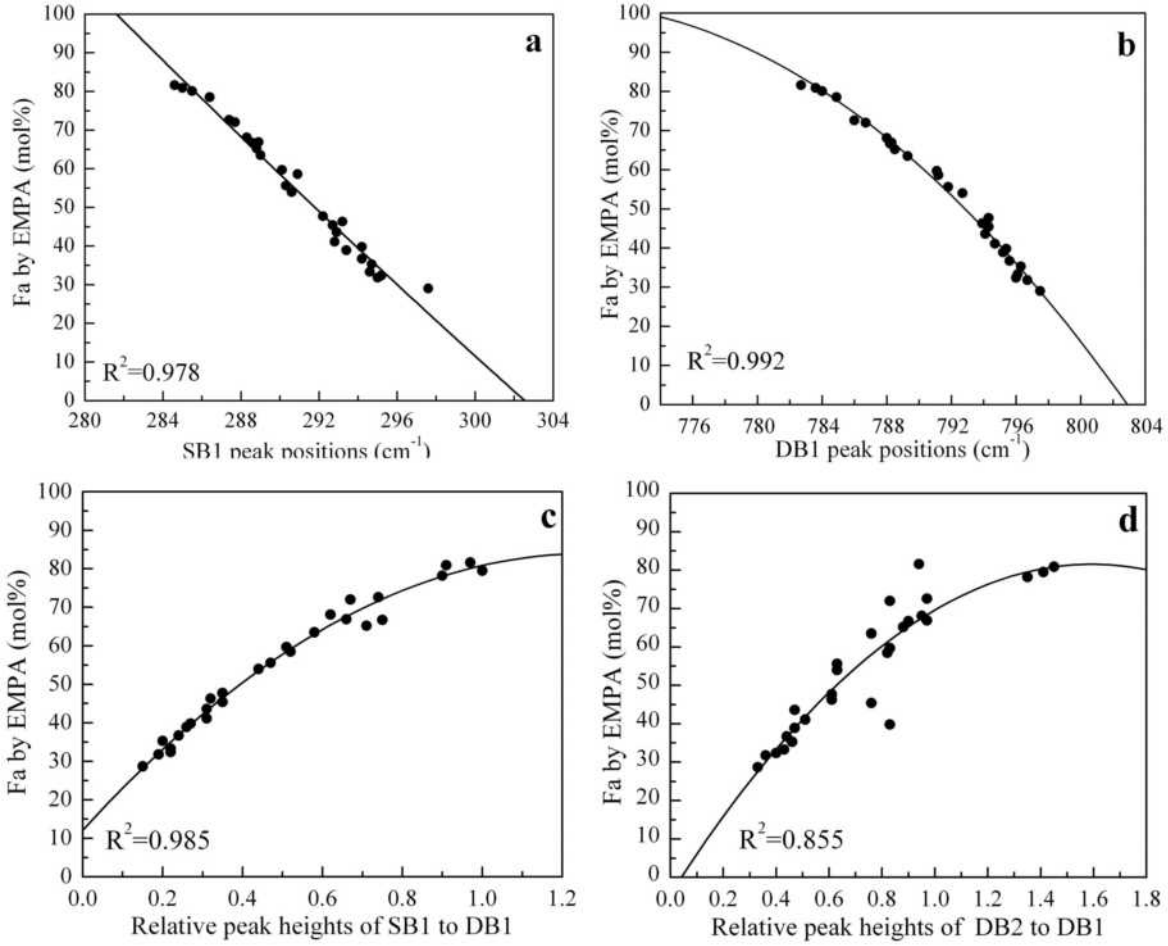

FIGURE 5. Correlations between chemical composition and Raman spectra criteria from the selected data set. Peak positions of (**a**) SB1 and (**b**) DB1 peak positions, and relative peak heights of (**c**) SB1 to DB1 and (**d**) DB2 to DB1 vs. the Fa values determined by EMPA. Both (**c**) and (**d**) show variation trends in correspondence to Fa values. However, in the full data set, the trends are much more scattered than the Raman peak positions of SB1 and DB1. Therefore, the relative Raman peak heights are not used to gauge the Fa contents of ringwoodite.

TABLE 3. Intercepts and coefficients for Eqs. 1–3

Equation (*i*)	y_i	a_i	b_i	c_i	d_i
1	2546.39518	−12.32257	0.01291		
2	−48186.57159	125.82885	−0.08197		
3	27.22299	80.28798	−26.07141	−0.13991	0.01460

These two single-peak calibrations were also applied to the full data set to test how accurate they can determine the compositions (Figs. 6c and 6d). As expected from the selected data set, the Fa values calculated from DB1 match better with the EPMA analyses than those from SB1. Both of these methods can predict the Fa contents of ringwoodite with an accuracy of approximately ±5 mol%. However, large scatter for Fe-poor grains (Fa < 30) were noticed in the two calibrations. It seems that the results may be underestimated by 6.4 mol% using SB1, and overestimated by 7.0 mol% using DB1.

Two-peak calibration

Similar to the method presented by Kuebler et al. (2006), the Fa contents of ringwoodite can be calibrated to both SB1 and DB1. Figure 7a shows a three-dimensional plot of Fa content vs. peak positions of SB1 and DB1 using the selected data set. The calibration equation from these plots yields a best-fit hyperbolic paraboloid, which is shown in Figure 7b. The paraboloid has the form as in Equation 3:

$$\text{Fa (SB1\&DB1)} = y_4 + a_4x_1 + b_4x_2 + c_4x_1^2 + d_4x_2^2 \quad (3)$$

where x_1 is the SB1 peak position, x_2 is the DB1 peak position, y_4 is the intercept, and a_4, b_4, c_4, and d_4 are, respectively, the coefficients listed in Table 3.

By projecting the best-fit paraboloid onto the plane of SB1 and DB1 peak positions, Fa value "contours" can be drawn (dashed lines in Fig. 8), as Fa = 10 or 20, etc. The Raman peak positions from the selected data set and full data set were plotted as well (Figs. 8a and 8b). The central curved solid lines are the best-fit parabola of these data points. Spreading in the range of $Fa_{30–50}$ from both data sets was noticed, which can be attributed to the deviation in SB1 peak positions. In addition, the Fe-rich points scatter into two clusters at the bounds of $Fa_{70–80}$.

The SB1 and DB1 peak positions of the selected data set were used with Equation 3 to find the Fa values predicted by the two-peak calibration and plotted against the Fa values of the corresponding EMPA data (Fig. 9a). The regression approximates a 1:1 correlation and the multi-correlation coefficient is 0.995,

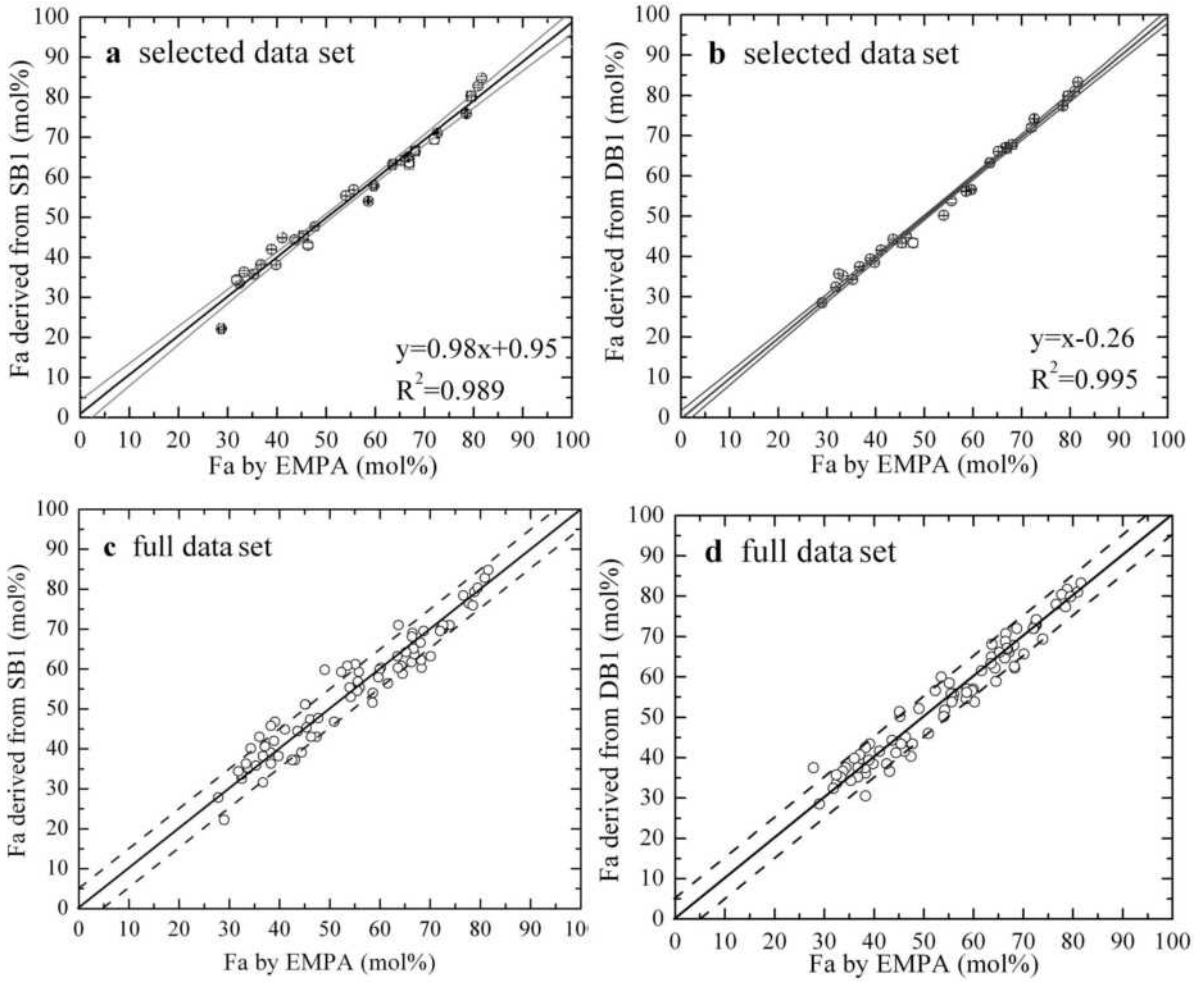

FIGURE 6. Fayalite values derived from the selected data set SB1 (**a**) and DB1 (**b**) single-peak calibrations plot against the Fa content determined by EMPA. The bold lines are the linear regressions, and the thin lines are 95% confidence intervals. The error bars are less than or equal to the size of symbols used for most data points. Full data set SB1 (**c**) and DB1 (**d**) are also plotted for comparison. The dotted lines indicate a range of ±5% Fa unit.

which is comparable to that of the DB1 calibration. However, the intercept of regression line of DB1 (0.26) is lower than that of the two-peak calibration (0.36). Minor discrepancies were observed on ringwoodite grains with Fa contents lower than 50 mol% ($Fa_{30–50}$) by the two-peak calibration (Fig. 9a), which is also shown as spread in this range on Figures 8a and 8b.

The calculated results vs. EMPA analyses of the full data set (Fig. 9b) show that there is no significant improvement with using the two-peak calibration with respect to the DB1 peak calibration. However, it is possible to estimate the compositions of ringwoodite within an accuracy of ±5 mol% by using either the DB1 single-peak or the SB1-DB1 two-peak calibration.

VIBRATIONAL MODES OF RINGWOODITE

To understand the structural stability of ringwoodite, the thermodynamic properties and lattice vibration of γ-M_2SiO_4 (M = Mg, Ni, Co) have been widely studied (Sung and Burns 1978; Lazewski et al. 2001; Price et al. 1987; Ringwood and Major 1970; Ringwood 1991). Assignments of the vibrational modes of IR and Raman spectra have been discussed by many authors (e.g., Jeanloz 1980; Akaogi et al. 1984; McMillan 1984; Guyot et al. 1986; McMillan and Akaogi 1987; Yamanaka and Ishii 1986; Chopelas et al. 1994). The strongest doublets of γ-Mg_2SiO_4 (DB1 and DB2 in this study) were assigned, respectively, to the symmetric (ν_1) and asymmetric (ν_3) stretching of the tetrahedral SiO_4 units (McMillan and Akaogi 1987), which was further revised with the 796 cm^{-1} band assigned to ν_3-derived F_{2g} mode and 835 cm^{-1} to ν_1-derived A_{1g} asymmetry (Chopelas et al. 1994). However, since the silicate spinels have the most regular SiO_4 tetrahedra, the vibration modes of the SiO_4 units exhibit the least amount of ν_1-ν_3 coupling (Piriou and McMillan 1983; McMillan 1984; McMillan and Akaogi 1987).

Although the ν_3-derived DB1 mode was considered as an essentially pure Si-O stretching mode (Preudhoome and Tarte 1972), which suggests the mode frequency should not vary significantly with cation substitution, there were measurable variations of peak positions in previous studies on silicate spinels. Nevertheless, very few studies have been devoted to the effects of cation substitution on vibrational motions. The Si-O stretching frequency (ν_3) was attributed to the cation-oxygen (M-O) distance based on study of infrared spectra of γ-Fe_2SiO_4, γ-Ni_2SiO_4, and γ-Co_2SiO_4 (Jeanloz 1980), or namely, the unit-cell size since the Raman frequencies in γ-Mg_2SiO_4, γ-Ni_2SiO_4, and γ-Co_2SiO_4 vary with cell dimension (Chopelas et al. 1994). The correlation between the ν_3-derived DB1 frequencies and Mg-Fe substitution ratios in natural ringwoodite from this study further

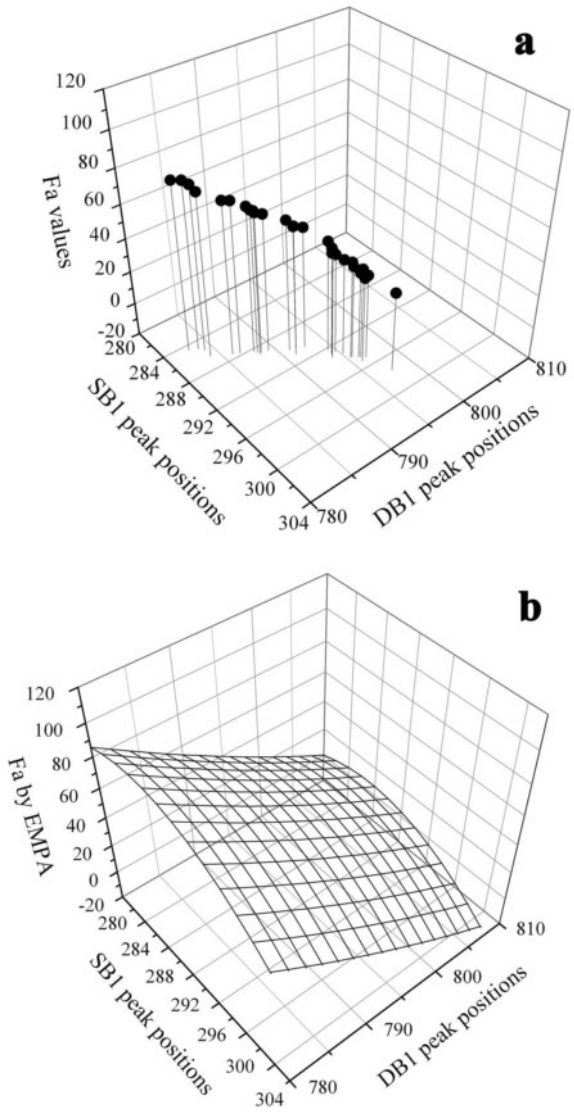

FIGURE 7. (**a**) Three dimensional plot of Fa contents vs. wavenumbers of SB1 and DB1. (**b**) The best-fit parabola for the two-peak calibration.

confirm the assumption that the octahedral cation has a strong influence on the ν_3 Si-O stretching.

Variation of the lowest energy mode (SB1 in this study) was observed in both synthesized silicate spinels and natural ringwoodite. In analogy with calculations on Ni_2SiO_4 spinel (Yamanaka and Ishii 1986), this peak was assigned to the F_{2g} translational mode of SiO_4 (McMillan and Akaogi 1987). Substitution of Ni^{2+} for Mg^{2+} causes the SB1 peak to shift to lower wavenumbers (from 302 to 190 cm^{-1} in frequency) and the shifted wavenumber can be estimated by the reduced mass ratio of m_{Ni}/m_{Mg} (McMillan and Akaogi 1987). This suggests that the F_{2g} mode is predominantly associated with motion of the octahedral cations rather than the translation of the SiO_4 tetrahedron. In this case, the SB1 peak of γ-Fe_2SiO_4 should also be around 190 cm^{-1}, as the mass of Fe (59 amu) is close to that of Ni (56 amu). However, the SB1 peak position of γ-Fe_2SiO_4 predicted by using our calibration equations is ~281 cm^{-1}, which is nearly 100 wavenumbers higher than that of γ-Ni_2SiO_4. This suggests that the effects on the SB1 vibration frequency are more complicated than previously thought, as the different types of translations in these cubic minerals are strongly coupled (Hofmeister and Chopelas 1991).

By analogy to Fe-Mg olivine, it was expected that DB2, the strongest doublet in ringwoodite Raman spectra, should show a good correlation with the Fa content. However, the variation of DB2 peak position exhibits little correlation with the chemical composition. One possibility is that this vibration is affected more by other factors (e.g., the randomly distributed crystal orientations) rather than chemical composition of ringwoodite. It can be demonstrated that this vibrational frequency does not vary significantly among γ-Mg_2SiO_4 (834 cm^{-1}), γ-Ni_2SiO_4 (848 cm^{-1}), and γ-Co_2SiO_4 (838 cm^{-1}), nor does it show any correlation with the cation mass (Chopelas et al. 1994). Accordingly, it is better to use SB1 and/or DB1 to estimate the chemical composition of ringwoodite from natural rocks.

The main factors that affect Raman peak intensity include the polarizability and symmetry of a crystal (Haskin et al. 1997). The relative peak heights of the strongest doublet in olivine (peak ~820 to peak ~840 cm^{-1}), which seem to decrease in the fayalite-forsterite series in unpolarized Raman spectra (Kuebler et al. 2006), were mainly attributed to the crystal orientations (Iishi 1978; Chopelas 1991; Kuebler et al. 2006). However, since SB1 and DB1 of ringwoodite belong to the same symmetry class, F_{2g}, it

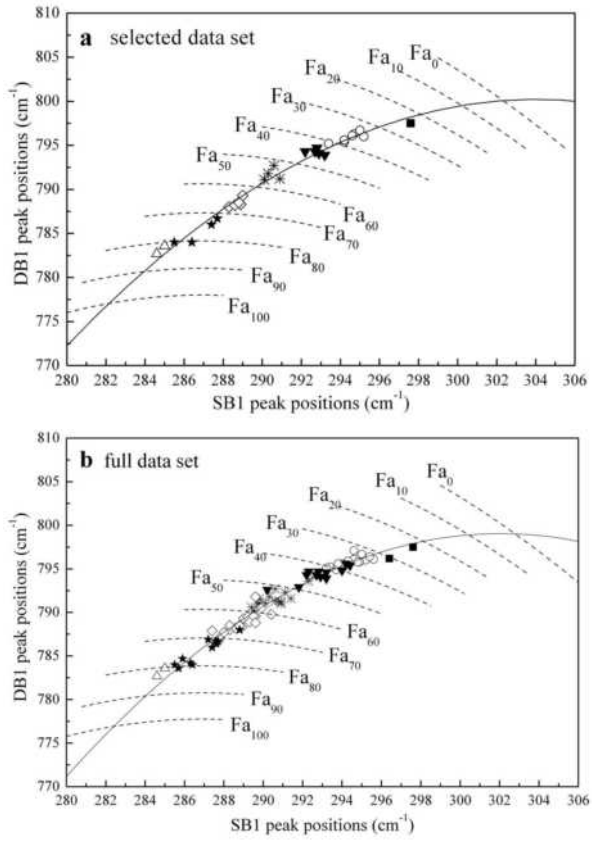

FIGURE 8. Two-dimensional projections of the peak positions from (**a**) the selected data set and (**b**) the full data set onto the plane of SB1 and DB1 peak positions.

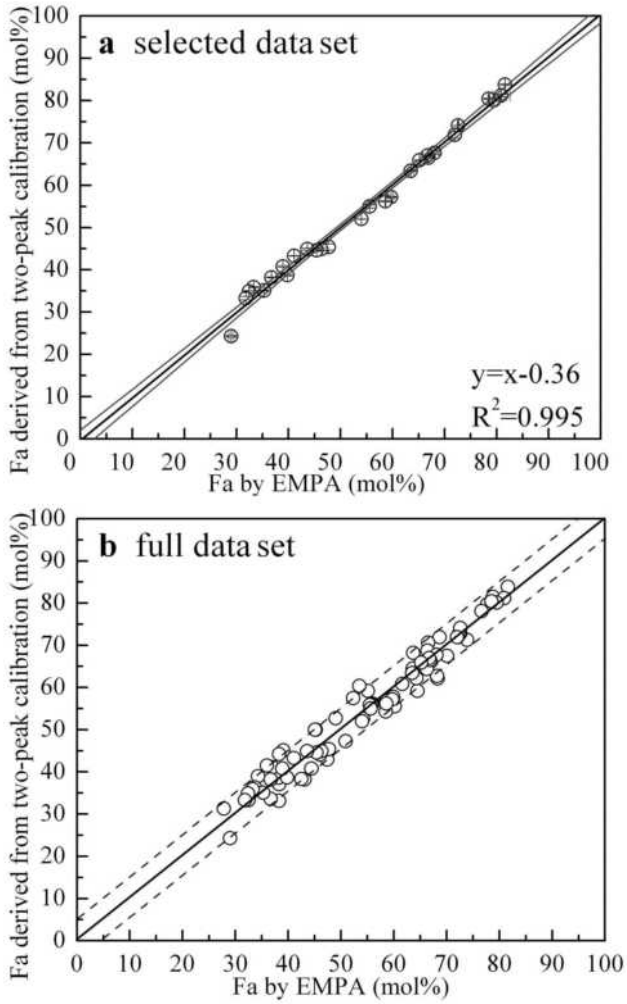

FIGURE 9. Fayalite values derived from the two-peak calibration plotted against the Fa content determined by EMPA. (**a**) Selected data set. Solid black line is linear regression and solid gray lines are 95% confidence intervals. The error bars are less than the size of symbols. (**b**) Full data set. The range of ±5 Fa units is outlined.

is expected that their relative intensities are independent of crystal orientations. The observed correlation between chemical compositions and relative peak heights of SB1 to DB1 is consistent with such a prediction. The increase of SB1 intensity that corresponds to the increase of Fe content suggests that the vibration of SB1 is enhanced with substitution of Mg^{2+} by Fe^{2+}.

POTENTIAL APPLICATIONS

The correlation between the Raman spectra and compositions of ringwoodite has the potential application of developing a technique for on-line measurement of the chemical composition of ringwoodite during diamond-anvil cell experiments. Ringwoodite grains that originated from solid-solid state transformation generally inherit homogeneous compositions from parental olivines (e.g., Putnis and Price 1979; Chen et al. 1996; Ohtani et al. 2004; Xie and Sharp 2007). However, recent studies on L-chondrites discovered ringwoodite grains that exhibit distinct chemical compositions (Miyahara et al. 2008, 2009; and this study), which suggest formation by fractional crystallization from an olivine melt. These reports require the study of fractional crystallization mechanisms of ringwoodite by high-pressure experiments. On-line measurement of the chemical composition of ringwoodite will be advantageous to reveal the fractional crystallization process in single runs, instead of carrying out a set of runs under certain pressure-temperature conditions. However, the effects of high pressure and temperature on the Raman spectra that have been studied and calibrated independently (Chopelas et al. 1994; Kleppe et al. 2002; Liu and Mernagh 1994; Liu et al. 1994, 2002) should also be considered.

Another important potential application will be in future space exploration missions including the Moon, terrestrial planets, and asteroids. Recently, calibrations of Raman spectra of many rock-forming minerals, e.g., olivine, low-Ca pyroxene and plagioclase, and Ti-Cr-oxides (ilmenite and chromite) have been developed (Freeman et al. 2003, 2008; Haskin et al. 1997; Kuebler et al. 2006; Wang et al. 2001, 2004). These calibrations supply us with the capability of simultaneous determinination of both crystal structure and chemical composition of minerals in situ on planetary or asteroidal surfaces using the Raman spectrometer (Laan et al. 2009; Perez and Martinez-Frias 2006; Sasaki et al. 2002; Sharma et al. 2002; Wang et al. 2003) alone. However, the results of Raman detection on rough rock/soil surfaces can be significantly affected by low signal/noise ratios and multiple mineral phases present in most spectra. To demonstrate the feasibility of this technique, Raman point-counting experiments were conducted on a rock chip of Martian meteorite, EETA 79001, and several methods (e.g., using both single-peak and two-peak calibrations) were also suggested to improve the reliability of the Raman-derived compositional estimates (Wang et al. 2004; Kuebler et al. 2006). The calibration of Raman spectra of ringwoodite extends this technique to high-pressure polymorphs, although more experiments and improvements in the technique are needed for its application in space missions in the future.

The common occurrence of ringwoodite in heavily shocked meteorites and the high density of craters on the Moon, Mars, and asteroids suggest the possible presence of ringwoodite when exploring the surface and subsurface of planets and asteroids. A highly promising site for detecting ringwoodite on the Moon is the South Pole Aitken (SPA) basin that was produced by catastrophic impact events (Lucey et al. 1998; Pieters et al. 1997) and which is up to 13 km in depth in some places (Zuber et al. 1994; Spudis et al. 1994). The bottom of the SPA basin may represent the lower lunar crust or possibly the lunar mantle (Lucey et al. 1998; Hammond et al. 2009; Pieters et al. 1997). Olivine-bearing gabbro was identified in the center of the basin by Clementine multispectral data (Pieters et al. 2001).

ACKNOWLEDGMENTS

We thank Ahmed El Goresy and associate editor Guoying Shen for reviews that led to improvements of this paper. The meteorite sample was supplied by the Polar Research Institute of China. Our study was supported by the Knowledge Innovation Program of the Chinese Academy of Sciences (kzcx2-yw-Q08, kzcx2-yw-110). L. Feng was also financially supported by Tohoku University Global COE program "Global Education and Research Center for Earth and Planetary Dynamics" and the Max-Planck Society.

REFERENCES CITED

Agee, C.B. (1998) Phase transformations and seismic structure in the upper mantle and transition zone. In R.J. Hemley, Ed., Ultrahigh Pressure Mineralogy: Physics and Chemistyry of the Earth's Deep Interior, 37, p. 165–203. Reviews in Mineralogy, Mineralogical Society of America, Chantilly, Virginia.

Akaogi, M., Ross, N.L., McMillan, P., and Navrotsky, A. (1984) The Mg_2SiO_4 polymorphs (olivine, modified spinel and spinel)-thermodynamic properties from oxide melt solution calorimetry, phase relations, and models of lattice vibrations. American Mineralogist, 69, 449–512.

Chen, M., Sharp, T.G., El Goresy, A., Wopenka, B., and Xie, X. (1996) The majorite-pyrope + magnesiowüstite assemblage: Constraints on the history of shock veins in chondrites. Science, 271, 1570–1573.

Chopelas, A. (1991) Single crystal Raman spectra of forsterite, fayalite, and monticellite. American Mineralogist, 76, 1101–1109.

Chopelas, A., Boehler, R., and Ko, T. (1994) Thermodynamics and behavior of γ-Mg_2SiO_4 at high pressure: implications for Mg_2SiO_4 phase equilibrium. Physics and Chemistry of Minerals, 21, 351–359.

Feng, L. and Lin, Y. (2008) Extracting compositions from Raman spectra of ringwoodite in the heavily shocked Grove Mountains meteorites. Meteoritics and Planetary Science, 43, A43.

Feng, L., Lin, Y., Hu, S., Xu, L., and Miao, B. (2007) Assemblages of olivine polymorphs in Grove Mountains(GRV) 052049: Constraints on pressure-temperature condition of shock metamorphism. Meteoritics and Planetary Science, 42, A45.

Freeman, J.J., Wang, A., Kuebler, K.E., and Haskin, L.A. (2003) Raman spectroscopic charaterization of the feldspars-implications for in situ surface mineral characterizationin planetary exploration. Lunar and Planetary Science, 1676.

Freeman, J.J., Wang, A., Kuebler, K.E., Joliff, B.L., and Haskin, L.A. (2008) Characterization of natural feldspars by Raman spectroscopy for future planetary exploration. The Canadian Mineralogist, 46, 1477–1500.

Potts, P.J. (1987) A Handbook of Silicate Rock Analysis, 622 p. Blackie, New York.

Guyot, F., Boyer, H., Madon, M., Velde, B., and Poirier, J.P. (1986) Comparison of the Raman microprobe spectra of $(Mg, Fe)_2SiO_4$ and Mg_2GeO_4 with olivine and spinel structures. Physics and Chemistry of Minerals, 13, 91–95.

Haskin, L.A., Wang, A., Rockow, K.M., Jolliff, B.L., Korotev, R.L., and Viskupic, K.M. (1997) Raman spectroscopy for mineral identification and quantification for in situ planetary surface analysis: a point count method. Journal of Geophysics Research, 102, 19293–19306.

Hammond, N.P., Nimmo, F., and Korycansky, D. (2009) Hydrocode Modeling of the South Pole Aitken Basin-Forming Impact. 40th Lunar and Planetary Science Conference, P1455.

Hofmeister, A.M. and Chopelas, A. (1991) Vibrational spectroscopy of end-member silicate garnets. Physics and Chemistry of Minerals, 17, 503–526.

Jeanloz, R. (1980) Infrared spectra of olivine polymorphs: α, β phase and spinel. Physics and Chemistry of Minerals, 5, 327–341.

Katsura, T. and Ito, E. (1989) The system Mg_2SiO_4-Fe_2SiO_4 at high pressures and temperatures: Precise determination of stabilities of olivine, modified spinel, and spinel. Journal of Geophysical Research, 94, 15663–15670.

Kuebler, K.E., Jolliff, B.L., Wang, A., and Haskin, L.A. (2006) Extracting olivine (Fo–Fa) compositions from Raman spectral peak positions. Geochimica et Cosmochimica Acta, 70, 6201–6222.

Kleppe, A.K., Jephcoat, A.P., and Smyth, J.R. (2002) Raman spectroscopic study of hydrous γ-Mg_2SiO_4 to 56.5 GPa. Physics and Chemistry of Minerals, 29, 473–476.

Iishi, K. (1978) Lattice dynamics of forsterite. American Mineralogist, 63, 1198–1208.

Laan, E.C., Westrenen, W.V., Wielders, A., Heiligers, J., and MoonShot partners (2009) MOONSHOT: A combined Raman / LIBS instrument for lunar exploration. 40th Lunar and Planetary Science Conference, P1836.

Lazewski, J., Jochym, P.T., Parlinski, K., and Piekarz, P. (2001) Lattice dynamics of Mg_2SiO_4. Journal of Molecular Structure, 596, 3–6.

Liu, L.G. and Mernagh, T.P. (1994) Raman spectra of high-pressure polymorphs of Mg_2SiO_4 at various temperatures. High Temperature-High Pressure, 26, 185–193.

Liu, L.G., Mernagh, T.P., and Irifune, T. (1994) High-pressure Raman-spectra of β-Mg_2SiO_4, γ-Mg_2SiO_4, $MgSiO_3$-ilmenite and $MgSiO_3$-preovskite. Journal of Physics and Chemistry of Solids, 55, 185–193.

Liu, L.G., Lin, C.-C., Mernagh, T.P., and Inoue, T. (2002) Raman spectra of hydrous γ-Mg_2SiO_4 at various pressures and temperatures. Physics and Chemistry of Minerals, 29,181–187.

Lucey, P.G., Taylor, G.J., Hawke, B.R., and Spudis, P.D. (1998) FeO and TiO_2 concentrations in the South Pole-Aitken basin: Implications for mantle composition and basin formation Journal of Geophysical Research, 103, 3701–370.

McMillan, P. (1984) Structural studies of silicate glasses and melts-applications and limitations of Raman spectroscopy. American Mineralogist, 69, 622–644.

McMillan, P. and Akaogi, M. (1987) Raman spectra of β-Mg_2SiO_4 (modified spinel) and γ-Mg_2SiO_4 (spinel). American Mineralogist, 72, 361–364.

Miyahara, M., El Goresy, A., Ohtani, E., Kimura, M., Ozawa, S., Nagase, T., and Nishijima, M. (2009) Fractional crystallization of olivine melt inclusion in shock-induced chondritic melt vein. Physics of the Earth and Planetary Interiors, 177, 116–121.

Miyahara, M., El Goresy, A., Ohtani, E., Nagase, T., Nishijima, M., Zahra Vashaei, Z., Ferroir, T., Gillet, Ph., Dubrovinsky, L., and Simionovici, A. (2008a) Evidence for fractional crystallization of wadsleyite and ringwoodite from olivine melts in chondrules entrained in shock-melt veins. Proceedings of the National Academy of Sciences, 105, 8542–8547.

Miyahara, M., Sakai, T., Ohtani, E., Kobayashi, Y., Kamada, S., Kondo, T., Nagase, T., HoYoo, J., Nishijima, M., and Vashaei, Z. (2008b) Application of FIB system to ultra-high-pressure Earth Science. Journal of Mineralogical and Petrological Sciences, 103, 88–93.

Mouri, T. and Enami, M. (2008) Raman spectroscopic study of olivine-group minerals. Journal of Mineralogical and Petrological Sciences, 103, 100–104.

Ohtani, E., Kimura, Y., Kimura, M., Takata, T., Kondo, T., and Kubo, T. (2004) Formation of high-pressure minerals in shocked L6 chondrite Yamato 791384: constraints on shock conditions and parent body size. Earth and Planetary Science Letters, 227, 505–515.

Perez, F.R. and Martinez-Frias, J. (2006) Raman spectroscopy goes to Mars. Spectroscopy Europe, 18, 18–21.

Pieters, C.M., Tompkins, S., Head, J.W., and Hess, P.C. (1997) Mineralogy of the mafic anomaly in the South Pole-Aitken Basin: Implications for excavation of the lunar mantle. Geophysical Research Letters, 24, 1903–1906.

Pieters, C.M., Head, J.W., Gaddis, L., Jolliff, B., and Duke, M. (2001) Rock types of South Pole-Aitken basin and extent of basaltic volcanism. Journal of Geophysical Research, 106, 28001–28022.

Piriou, B. and McMillan, P. (1983) The high-frequency vibrational spectra of vitreous and crystalline orthosilicates. American Mineralogist, 68, 426–443.

Preudhoome, J. and Tarte. P. (1972) Infrared studies of spines-IV Normal spinels with a high-valency tetrahedral cation. Spectrochimica Acta, 28A, 69–79.

Price, G.D., Parker, S.C., and Leslie, M. (1987) The lattice dynamics and thermodynamics of the Mg_2SiO_4 polymorphs. Physics and Chemistry of Minerals, 15, 181–190.

Putnis, A. and Price, G.D. (1979) High-pressure $(Mg,Fe)_2SiO_4$ phases in the Tenham chondritic meteorite. Nature, 280, 217–218.

Ringwood, A.E. (1991) Phase-transformations and their bearing on the constitution and dynamics of the mantle. Geochimica et Cosmochimica Acta, 55, 2083–2110.

Ringwood, A.E. and Major, A. (1970) The system Mg_2SiO_4-Fe_2SiO_4 at high pressures and temperatures Physics of The Earth and Planetary Interiors, 3, 89–108.

Sasaki, S., Kubota, T., Okada, T., Saiki, K., Kuroda, Y., Kunii, Y., Shibamura, E., Akiyama, N., Ohtake, M., Ichikawa, M., and others. (2002) Scientific exploration of lunar surface using a rover in Japanese future lunar mission. Advance in Space Research, 30, 1921–1926.

Sharma, S.K., Angel, S.M., Ghosh, M., Hubble, H.W., and Lucey, P.G. (2002) Remote pulsed laser Raman spectroscopy system for mineral analysis on planetary surfaces to 66 meters. Applied Spectroscopy, 56, 699–705.

Spudis, P.D., Reisse, R.A., and Gillis, J.J. (1994) Ancient multiring basins on the Moon revealed by Clementine Laser Altimetry. Science, 266, 1848–1851.

Sung, C.-M. and Burns, R.G. (1978) Crystal structural features of the olivine → spinel transition. Physics and Chemistry of Minerals, 2, 177–197.

Wang, A., Jolliff, B.L., Haskin, L.A., Kuebler, K.E., and Viskupic, K.M. (2001) Characterization and comparison of structural and compositional features of planetary quadrilateral pyroxenes by Raman spectroscopy. American Mineralogist, 86, 790–806.

Wang, A., Kuebler, K.E., Jolliff, B.L., and Haskin, L.A. (2004) Raman spectroscopy of Fe-Ti-Cr-oxides, case study: Martian meteorite EETA79001. American Mineralogist, 89, 665–680.

Wang, A., Haskin, L.A., Lane, A.L., Wdowiak, J.T., Squyres, S.W., Wilson, R.J., Hovland, L.E., Manatt, K.S., Raouf, M., and Smith, C.D. (2003) Development of the Mars microbeam Raman spectrometer (MMRS). Journal of Geophysical Research, 108, 5005.

Xie, Z. and Sharp, T.G. (2007) Host rock solid-state transformation in a shock-induced melt vein of Tenham L6 chondrite. Earth and Planetary Science Letters, 254, 433–445.

Yamanaka, T. and Ishii, M. (1986) Raman scattering and lattice vibrations of Ni_2SiO_4 spinel at elevated temperature. Physics and Chemistry of Minerals, 13, 156–160.

Zuber, M.T., Smith, D.E., Lemoine, F.G., and Neumann, G.A. (1994) The shape and internal structure of the Moon from the Clementine Mission. Science, 266, 1839–1843.

MANUSCRIPT RECEIVED AUGUST 24, 2010
MANUSCRIPT ACCEPTED MAY 31, 2011
MANUSCRIPT HANDLED BY GUOYIN SHEN